Carbon 159 (2020) 412–421

Contents lists available at ScienceDirect

Carbon

journal homepage: www.elsevier.com/locate/carbon

Crosslink-tuned large-deformation behavior and fracture mode in buckypapers

Tian Yang [a, b], Chao Wang [a, b, *], Zuobing Wu [a, b, *]

[a] LNM, Institute of Mechanics, Chinese Academy of Sciences, Beijing, 100190, China
[b] School of Engineering Science, University of Chinese Academy of Sciences, Beijing, 100049, China

ARTICLE INFO

Article history:
Received 30 September 2019
Received in revised form
21 November 2019
Accepted 16 December 2019
Available online 18 December 2019

Keywords:
Strongly-crosslinked buckypaper
Crosslink
Deformation mode
Ductile-brittle transition
Coarse-grained molecular dynamics

ABSTRACT

Strong physical and/or chemical inter-tube crosslinks play a vital role in carbon nanotube buckypapers and composites. However, both underlying mechanisms and regulation patterns remain poorly understood. Here, we employed the coarse-grained molecular dynamics simulations to investigate the nonlinear large-deformation behavior and the fracture mode of crosslinked buckypapers by considering both intrinsic intra- and inter-tube bond-breaking. A critical crosslink density ρ_c is found to divide the deformation mode of buckypaper into two regimes in uniaxial tension, *i.e.*, the bending-dominated mode at $\rho < \rho_c$ and the bending-stretching-bending three-stage one at $\rho > \rho_c$. This transition is attributed to the stress concentration and the intrinsic bond-breaking in large tensile deformations. In uniaxial compression, it is always bending-dominated, which is independent of crosslinks and compressive strain. Furthermore, there exists another critical crosslink density controlling the ductile-brittle transition of fracture mode of the strongly-crosslinked buckypaper, which is explained from the viewpoint of the collective hierarchical microstructural evolution. This study provides a profound understanding of crosslink effect on the buckypaper, which is of great significance for the optimization design and further practical applications of the promising material.

1. Introduction

Buckypaper is a typical nano-porous thin-film material, in which carbon nanotubes (CNTs) are randomly distributed and arranged into a nonwoven fibrous structure, as ordinary paper made from wood pulp fibers [1]. Because of the combined advantages of both porous materials and 1D CNTs, it possesses advantages over high porosity [2], enhanced thermal [3], electrical [4] and mechanical properties [5–8], which enables its applications in multiple fields, such as high-performance composites [9], electrode materials [10], filtrations [11] and multifunctional devices [12,13].

Since the first free-standing buckypaper was fabricated by Liu et al. [14] in 1998, it has been realized that the mechanical properties of buckypaper are greatly influenced by the interfacial strength of contacted CNT fibers [15,16]. Many experimental schemes have been proposed to strengthen inter-tube connections in buckypaper for better mechanical properties, which falls into two main categories: the physical-adhesion-based strategy and the chemical-bonding-based one. For the former, various heterogeneous micro/nano additives, such as polymeric adhesives [17], polyacrylonitrile [18], graphene nanosheets [19] have been intercalated into the porous skeleton of buckypaper; these additives prefer to agglomerate and locate around CNT joints [20], which increases effective inter-tube areas and strengthens interfacial connections like glue. For example, Coleman et al. [17] used polymeric adhesives to intercalate buckypaper and obtained the Young's modulus, strength, and toughness increased by factors of 3, 9, and 28, respectively. For the latter, the methods of nitrene reaction [21], electron-beam irradiation [22] and/or chemical functionalization [23] have been adopted to introduce strong chemical bonds between neighbor fibers in buckypapers to achieve enhanced mechanical properties. *E.g.*, Jakubinek et al. [23] produced covalently crosslinked buckypaper by chemical functionalization to achieve 10 times stronger and stiffer than the pristine one. It is noted that not only mechanical properties, but electrical and thermal ones [7,23,24] of buckypaper can also been improved effectively by adding strongly physical and/or chemical crosslinks.

* Corresponding authors. LNM, Institute of Mechanics, Chinese Academy of Sciences, Beijing, 100190, China.
E-mail addresses: wangchao@lnm.imech.ac.cn (C. Wang), wuzb@lnm.imech.ac.cn (Z. Wu).

https://doi.org/10.1016/j.carbon.2019.12.037
0008-6223/

It has been widely accepted that the strongly-crosslinked buckypaper (SCBP) is more applicable than its precursor of pristine buckypaper (PBP) [25,26].

Extensive numerical/experimental researches have been dedicated to uncover the relationship between macroscopic properties and microstructural/topological characteristics of PBP. For example, using coarse-grained molecular dynamics method (CGMD), Xie et al. [27] identified the characteristics of microstructural evolution of pristine buckypapers, *i.e.*, bundling, bridging and aligning. Cranford et al. [28] found that the Young's modulus is tunable over a range of approximately 0.2–3.1 GPa by changing nanotube type and density of PBP. Li et al. [1] illustrated the stiffness of buckypaper decreases with the increment of tube length as the density of buckypaper is reduced. Chen et al. [29] reported that buckypaper with higher density has larger dynamic stiffness and a higher loss factor up to ~0.29. Wang et al. [30] further showed that viscoelastic properties of buckypaper is temperature- and loading frequency-invariant and can be improved effectively by pre-strain. By performing *in situ* tensile loading, Ma et al. [31] revealed the in-plane Poisson's ratios of PBP changed from negative to positive, which lies in the elongation of bending CNTs and the angle variation between CNTs, respectively. As far as we know, only Berhan et al. [32], Xie et al. [27] and Chen et al. [33] studied the effect of strong crosslinks on the mechanical properties of SCBP. Berhan et al. [32] performed simulations to study the effect of crosslink morphology on the stiffness of SCBP and concluded that crosslinks at each fiber joint could increase effective moduli by a factor of ~2.5–30. Xie et al. [27] studied the uniaxial tensile deformation behavior of SCBP using CGMD method, and found that the network topology has negligible change in tension due to the restriction effect of strong crosslinks and the stress distribution is uniform throughout the network in the tensile direction. Chen et al. [33] found that there exist two critical network densities which divide the stiffness behavior into three stages: zero stiffness, bending dominated and stretching dominated through theoretical analysis.

However, all of these computational/theoretical models of SCBP are rather ideal, the bond-breaking which would definitely occur in the large deformation of SCBP in experiments [34–37] has not been embedded in these models, as a result, the intrinsic characteristics of large deformation and the corresponding micro-, meso- and macroscopic fractures have not been captured in these researches. So, the underlying mechanism of large-deformation and the corresponding multiscale fracture of SCBP remain elusive, such as what is the effect of strong crosslinks on the deformation mode of SCBP in large deformation? Whether it's stretching dominated or bending dominated or some other types? What is the fracture mode of SCBP in large deformation, ductile or brittle?

In the present work, a mesoscopic SCBP model (Fig. 1a and b) is designed to systematically evaluate the effect of strong inter-tube crosslinks based on the CGMD, in which crosslinks are randomly distributed. Here, the inter-tube crosslink (Fig. 1c) is used to simulate the realistic strong connections due to the physical adhesion and/or chemical bonding as observed by SEM and TEM in Fig. 1d. Fig. 1d–i shows a SEM image of Y-type junctions (in red circles) formed during preparation [34], which is a kind of physical-adhesion-based crosslink. Fig. 1d–ii, d-iii are TEM images of chemically crosslinked carbon nanotubes extracted from the irradiated buckypaper [22], in which red arrows mark inter-tube crosslinks formed after e-beam irradiation. In our simulations, the crosslink density ρ is defined as the average number of crosslinks per coarse-grained CNT chain, which equals 10 in Fig. 1a and is tuned in simulations. Unless specified otherwise, the inter-tube crosslinks have the same mechanical properties with the intra-tube bonds as the tensile force-distance relationship given in Fig. 1e. The fracture strain of the intra/inter-tube bond is set to be 0.2 which is comparable to the experiments [38] and simulations [39]. Fig. 1f shows the rich mesoscopic configurations of crosslinked carbon nanotubes observed in numerical SCBP structures. Here, we mainly focus on the dynamic large deformation behavior of crosslinked buckypaper with the tensile strain of 1.2 and the compressive one of −0.98. See more information about the model and simulations in the second section. On the basis of the CG model, we reproduce the enhanced mechanical properties of crosslinked buckypaper under a tensile loading. In particular, we uncovered the tunable dominated deformation mode that changes from bending dominated to bending-stretching-bending three-stage transition with increasing crosslink density in large-strain tension. Furthermore, we unveiled the ductile-brittle transition mechanism of the SCBP with increased crosslink density, which is explained from the viewpoint of hierarchical microstructural evolution. The effect of other influencing factors, such as the bending stiffness of CNT fibers and the tensile stiffness of crosslinks are discussed as well.

2. Numerical model and methodology

2.1. Coarse-grained molecular dynamics

Since the CNT-based buckypaper is composed of a large number of CNTs and complex inner interactions, it is too expensive computationally to simulate the behaviors of SCBP using full-atom MD simulations. Here, CGMD is adopted to explore the mechanical behavior of buckypaper. A single carbon nanotube is represented by a bead-spring model consisting of a series of beads connected by springs, where the equivalent bonds are collective interaction of many bonds between real atoms studied in full-atom simulations. Force field interactions include internal bonds, angle springs and pair potentials. Therefore, the deformation energy can be calculated by tensile energy E_T, bending energy E_B, van der Waals energy E_{pairs} as given below

$$E_T = k_T (r\text{-}r_0)^2/2, \tag{1}$$

$$E_B = k_B (1+\cos\theta), \tag{2}$$

$$E_{pairs} = 4\varepsilon[(\sigma/r)^{12}\text{-}(\sigma/r)^6], \tag{3}$$

where k_T, k_B, θ, r, r_0 are the tensile stiffness, bending stiffness, the angle of the triplet, current bond length and the equilibrium one, respectively. ε and σ denote the energy well depth and the zero-energy distance. The cutoff applied to non-bonded pair interactions is 3 nm. The bond would break as its tensile strain exceeds a critical value as shown in Fig. 1e. The reliability of this approach has been verified in previous studies [27–30,40,41].

The parameters of main force field used in this simulation are listed in Table 1, which were calibrated from full-atom MD simulation. More details about the coarse-grained scheme of carbon nanotubes can be found in Refs. [28,42]. All simulations are based on the large-scale atomic/molecular massively parallel simulator (LAMMPS) [43]. And the results are visualized based on the Open Visualization Tool (OVITO) [44].

2.2. Fabrication of numerical samples

Numerical models are established by randomly generating 100 carbon nanotubes with the contour length of 100 nm. Each of them has an initial curvature to reflect the semiflexible characteristics and direction fluctuation. These nanotubes are first deposited layer by layer to form loose buckypaper samples. To accelerate this process, a rigid substrate is added at the bottom of the simulation box and a body force is applied downward along the z direction. A

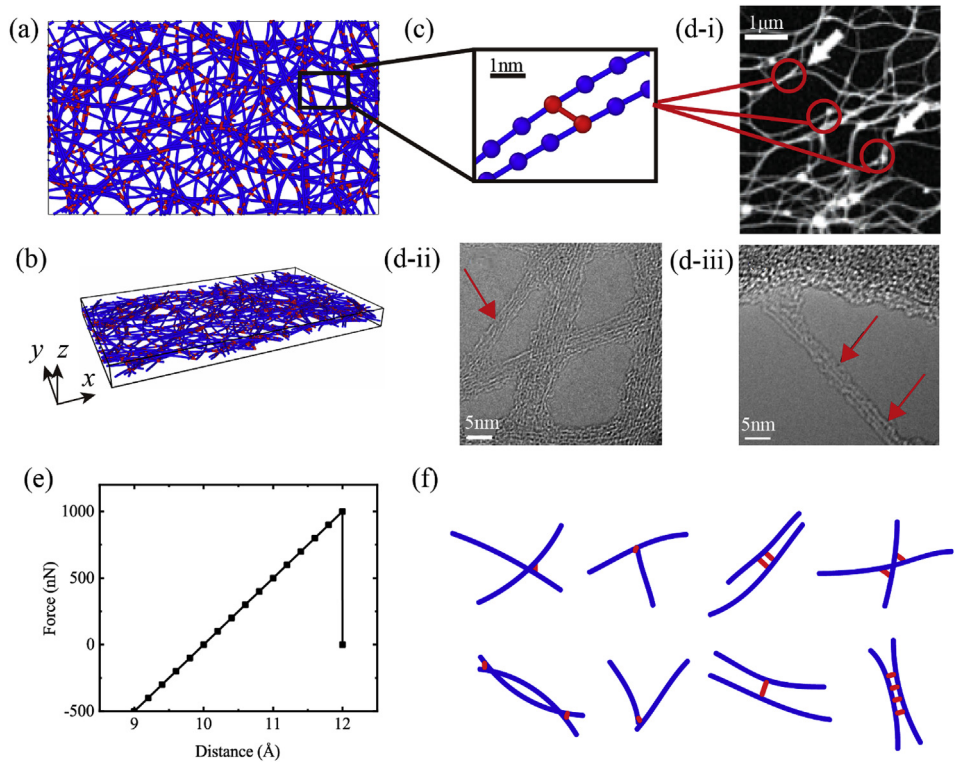

Fig. 1. Schematic of SCBP and corresponding microstructures. (a) The top view of the numerical sample (carbon nanotubes are in blue, crosslinks are in red) with the crosslink density of 10. (b) The 3D view of the sample. (c) The enlarged view of a crosslink connecting two adjacent nanotubes. (d) Experimental images of inter-tube crosslinks in buckypapers. SEM image of Y-type junctions in red circles formed during preparation (d–i) [34]. TEM images of crosslinked carbon nanotubes extracted from the irradiated buckypaper (d-ii, d-iii) [22], where red arrows mark inter-tube crosslinks formed after e-beam irradiation. (e) The force-distance relationship of a single intra/inter-tube bond. (f) Mesoscopic configurations of crosslinked nanotubes in the CG model. (A colour version of this figure can be viewed online.)

Table 1
The parameters for a (5,5) carbon nanotube in the CGMD [20,28,45].

Parameters	Values
Equilibrium inter-bond distance r_0 (Å)	10
Tensile stiffness k_T (kcal mol^{-1} Å^{-2})	1000
Equilibrium angle α_0 (°)	180
Bending stiffness k_B (kcal/mol)	14300
Lennard-Jones parameter ε (kcal/mol)	15.1
Lennard-Jones parameter σ (Å)	9.35

Langevin thermostat [46] with 300 K and a Berendsen barostat with 0 Pa are taken in the isothermal-isobaric ensemble (NPT). Periodic boundary conditions are added both in the x and y directions, but a free one in the z direction. When the total energy fluctuation is less than 0.1%, the model is considered to be in equilibrium. Then the substrate and force are removed, and the pristine buckypaper is obtained. After that, a detection program is adopted to find out all adjacent coarse-grained beads within 0.9–1.1 nm, a range around the equilibrium length of 1 nm for bonds. Some pairs are then chosen randomly to generate crosslinks between the two beads in the pair according to the crosslinking degree. This process is corresponding to the experiments [17,36], in which a strongly crosslinked buckypaper is always made through two steps: a pristine buckypaper is first synthesized and then the strongly chemical and/or physical crosslinks are added between adjacent carbon nanotubes. The newly obtained numerical crosslinked buckypaper samples are exerted successively the geometrical optimization and the dynamic energy optimization at a Langevin thermostat with 300 K and a Berendsen barostat with 0 Pa in both x and y directions to obtain a well-equilibrated system with a convergent energy as shown in Fig. S1 in Supporting Information. The equilibrium density of the obtained network at the ambient condition is 0.28 g/cm^3, which is comparable to the network fabricated in the laboratory [47].

2.3. Uniaxial tensile/compressive loads

In order to investigate the mechanical behaviors and deformation mechanisms of the buckypaper under large deformation, a series of uniaxial tension and compression in strain-controlled monotonic loading are conducted based on our CG model. The tensile loading is applied along the x direction with the tensile strain rate of 8×10^7 s^{-1} to the final tensile strain of 1.2. For a compressive loading, the buckypaper is compressed to a strain of -0.98 at the compressive rate of 2×10^7 s^{-1}. The periodic boundary condition is adopted in both x and y directions of the system and it is left free in z direction. A constant temperature of 300 K and a zero-pressure barostat in y direction are adopted. The time step in our simulations is taken to be 10 fs.

3. Results and discussions

3.1. The deformation under uniaxial tensile/compressive loads

In order to investigate the effect of inter-tube crosslinks on the mechanical performance of buckypapers, we make a series of numerical samples with varied crosslink density ρ. Especially, the system without crosslinks ($\rho = 0$) is studied to compare with the system with crosslinks, and the effect of a wider range of $\rho = 1$ and 10 are investigated. The mechanical responses of three samples in

uniaxial tension are shown in Fig. 2. Fig. 2a displays their stress-strain relationship. The tensile stress for the samples with $\rho = 0$ and 1 increases slowly with the increased strain, and decreases gradually after reaching the peak value of stress. The difference is that the strength of the latter is higher than that of the former. For the sample with a large amount of crosslinks ($\rho = 10$), the tensile strength is almost 6 times higher than that of the sample without crosslinks ($\rho = 0$). This is qualitatively consistent with the experimental results [22,48] that the buckypaper would be strengthened after crosslinking. In addition, the ductility of the buckypaper is deteriorated as the increase of crosslink density, *e.g.*, the fracture strain is decreased greatly from 1.1 to 0.5 as ρ increases from 0 to 10. To test the reliability of the result, we produced three numerical samples independently for each given crosslink density and the similar stress-strain curves are obtained as shown in Fig. S2 in Supporting Information, which clearly shows that it is mainly the crosslink density that controls the mechanical responses.

The deformation of the buckypaper is greatly influenced by the crosslink density as shown in Fig. 2b. The transverse size L_y of the samples for both ρ=0 and 1 decreases monotonously with increasing tensile strain due to the Poisson effect, and the reduction of L_y for the buckypaper with ρ=1 is always smaller than that of the buckypaper without crosslinks because of the retention effect [23] of crosslinks. For the buckypaper with a large amount of crosslinks (ρ=10), the transverse size decreases more slowly than the other two samples with less crosslinks due to the stronger retention effect when the tensile strain $\varepsilon < 0.2$; then, with an increased tensile strain, the out-of-plane bending deformation occurs due to the relatively smaller out-of-plane bending resistance, leading to the drastic decrease of the transverse size as $0.2 < \varepsilon < 0.45$; at $\varepsilon = 0.45$, the SCBP damages locally as shown in the left corner of Fig. 2b, which causes the release of concentrated stress; after that, the transverse size rises and finally restores to the original value due to the complete fracture of buckypaper. In addition, the buckypaper

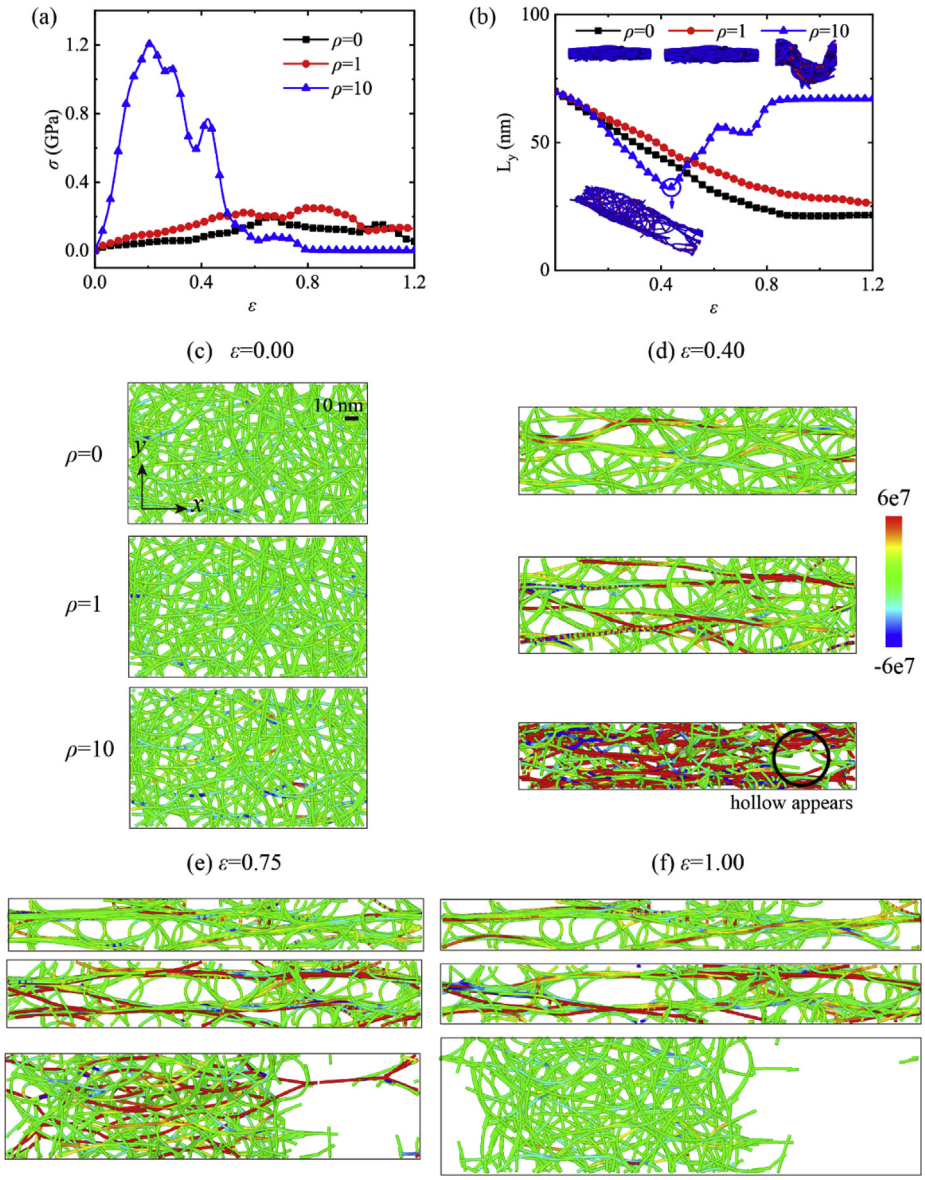

Fig. 2. The mechanical behavior of three structures with the crosslink density $\rho = 0, 1, 10$, respectively, under a uniaxial tensile loading. (a) The stress-strain curves. (b) The rule of transverse dimension L_y under large tensile deformation. (c–f) The stress contours of σ_{xx} as the strain is increased from 0.00 to 1.00. (A colour version of this figure can be viewed online.)

with smaller ρ (0 or 1) deforms only in the in-plane fashion, while the buckypaper with a large amount of crosslinks (ρ=10) undergoes out-of-plane bending owing to the crosslink effect as the side views shown in the upper side of Fig. 2b.

We also study the distribution and evolution of the components of the stress tensor σ in tension, as shown in Fig. 2c–f and Figs. S3–5. The definition of the local stress state of a discrete system is given in Supporting Information. At the initial state when the system has been well equilibrated for a long time with the total energy of the system converges as shown in Fig. S1, there is almost no stress concentration in the buckypaper without crosslinks, but the concentration of both tensile and compressive stress emerges gradually in the other two systems with larger crosslink density and it is more obvious for the sample with $\rho = 10$. When the buckypapers with $\rho = 0$ and 1 are stretched to a moderate strain of 0.40, most of the constituent nanotubes align horizontally along the loading direction and assemble to form thick bundles which bear relatively higher stress than other configurations of the system. For the system with an increased ρ of 10, some hollows appear locally as shown in Fig. 2d as a result of the bond breaking, which occurs after the local tensile strain of CNTs surpasses the critical value of 20%. Due to the restriction of massive crosslinks, no thick bundle along the tensile direction is formed and the buckypaper has both the in-plane approximately affine deformation and the out-of-plane paper-like bending as the inset shown in the upper side of Fig. 2b, which is much different from that in the buckypaper with less crosslinks. As the tensile strain further increases to 0.75, the topological structures as well as the stress distributions for the buckypapers with $\rho = 0$ and 1 evolve similarly with pores growing bigger and bundles becoming thicker. This state does not change too much even if the tensile strain is up to 1.0. However, things are much different for the system with $\rho = 10$, the hollow region observed before has nearly penetrated and the buckypaper is about to break as $\varepsilon = 0.75$, at the same time, many high stress states have been reduced greatly due to a large number of bond breaking; at last, the buckypaper is completely broken and the stress is nearly completely released as the strain is increased to 1.0. It is noted that the values of other five stress components are also higher for the system with larger crosslink density as shown in Figs. S3–5 in the Supporting Information.

Fig. 3 shows the deformation behavior of the buckypapers with three crosslink density of 0, 1 and 10 under uniaxial compressive loads. As shown in Fig. 3a, the stress-strain curves of all three samples exhibit similar U-shape characteristic, in which the stress increases sharply to a peak due to affine deformation in a much small compressive strain; then it falls and stabilizes immediately because of the relative sliding of constituent CNTs and the macroscopic out-of-plane bending as the typical morphologies shown in Fig. 3b when the compressive strain is 0.6; finally, the stress again increases sharply as the system is compacted at a large compressive strain. It is much interesting that, the constituent CNTs can slide freely relative to each other in a non-crosslinked network, causing an in-plane deformation in compression, however, even if a small amount of crosslinks ($\rho = 1$) are introduced into the system, the relative sliding of CNTs seems to be locked and the buckypapers would bend out-of-plane under compression and form a three-dimensional U-shape structure.

The distribution and evolution of the stress component σ_{xx} and other stress components under compressive loads are given in Fig. 3c–e and Figs. S6–8. The initial stress states for the three samples with $\rho = 0$, 1 and 10 are same with the corresponding one given in Fig. 2c; differently, there is no massive stress concentration during compression even at a moderate compressive strain of −0.5. All stress components maintain a small value in a wide range of compressive strain and increase greatly until the system is compacted to a large strain of −0.98 as shown in Fig. 3c–e and Figs. S6–8 in the Supporting Information.

The large deformation and fracture behaviors of buckypapers in uniaxial tension and compression are described by the combination of three constitutive relationships, i.e., the stretching-breaking of bonds, the bending of angles and the nonlinear van der Waals force for non-bonded pair interactions. We counted the distribution of the strain of all bonds in tension and compression as shown in Fig. S9, the strain of most bonds falls in the range of ±0.1 and ± 0.02, respectively, far less than the breaking strain of 0.2. So, the large deformation of the buckypaper is mainly due to the bending of CNTs and the relative sliding between them, the stretching strain of bonds is not large actually.

3.2. The dominated deformation mode and its tunability

In order to study the dominant deformation mode, we examine the energy ratio [49] defined as E_T/E_B, *i.e.*, the ratio of all stretching energy to all bending one. When the energy ratio is greater than 1, it indicates that the deformation of buckypaper is stretching dominated, or it is bending dominated. In addition, the failure extent is characterized by the ratio of broken bond, which is defined as the ratio of the number of broken bonds to the total bond number in the system. As shown in Fig. 4a, the energy ratio is smaller than 1 in the initial state of the four systems with $\rho = 0, 1, 3$ and 10. It remains smaller than 1 in the whole tension process for the system with $\rho = 0$ and 1, indicating that it is the bending dominated deformation for the buckypaper with less crosslinks. For the system with more crosslinks ($\rho = 10$), the energy ratio increases constantly and surpasses 1 as the tensile strain $\varepsilon > 0.15$, and it reaches the maximum value as $\varepsilon = 0.2$ when the first bond breaking event occurs as the dotted line denoted in Fig. 4a, after that, it decreases constantly to zero due to the continuous bond breaking as the tensile strain increases. That is to say, the deformation of the buckypaper with a large number of crosslinks shows a bending-stretching-bending three-stage pattern, a totally different rule. We find a critical crosslink density ρ_{cri} of ~3, which labels the transition of the deformation mode from bending-dominated to bending-stretching-bending three-stage fashion as shown in Fig. 4a. In uniaxial compression, the deformation is always dominated by CNT bending and no bond-breaking occurs during the whole process for all three systems with different crosslink density as shown in Fig. 4b. The transition of the deformation modes tuned by crosslinks in large deformations is much different from that studied in the small deformation of fiber network material [50], in which a crossover of deformation mode is expected from bending-dominated to stretching-dominated barely as crosslinks increase. This should be of vital importance to the understanding of analogous fiber network materials.

3.3. The ductile-brittle transition mechanism

We also investigate the effect of crosslinks on the fracture mode of the SCBP, which can be explained from the viewpoint of the collective hierarchical microstructural evolution. The stress-strain curves of the systems with $\rho = 1$, 5 and 15 as well as the curves of the ratio of broken bond are presented in Fig. 5a. These representative densities are the critical values of the following three typical fracture modes. For the buckypaper with $\rho = 1$, the tensile stress rises slightly, goes through linear elasticity and plastic yield platform, and reaches the peak value at the strain of 0.80, then drops slowly but never down to 0, meaning that this structure is not damaged completely and still has weak bearing capacity at the end. There is no broken bond during the whole loading process, indicating that the loss of bearing capacity is only related to the

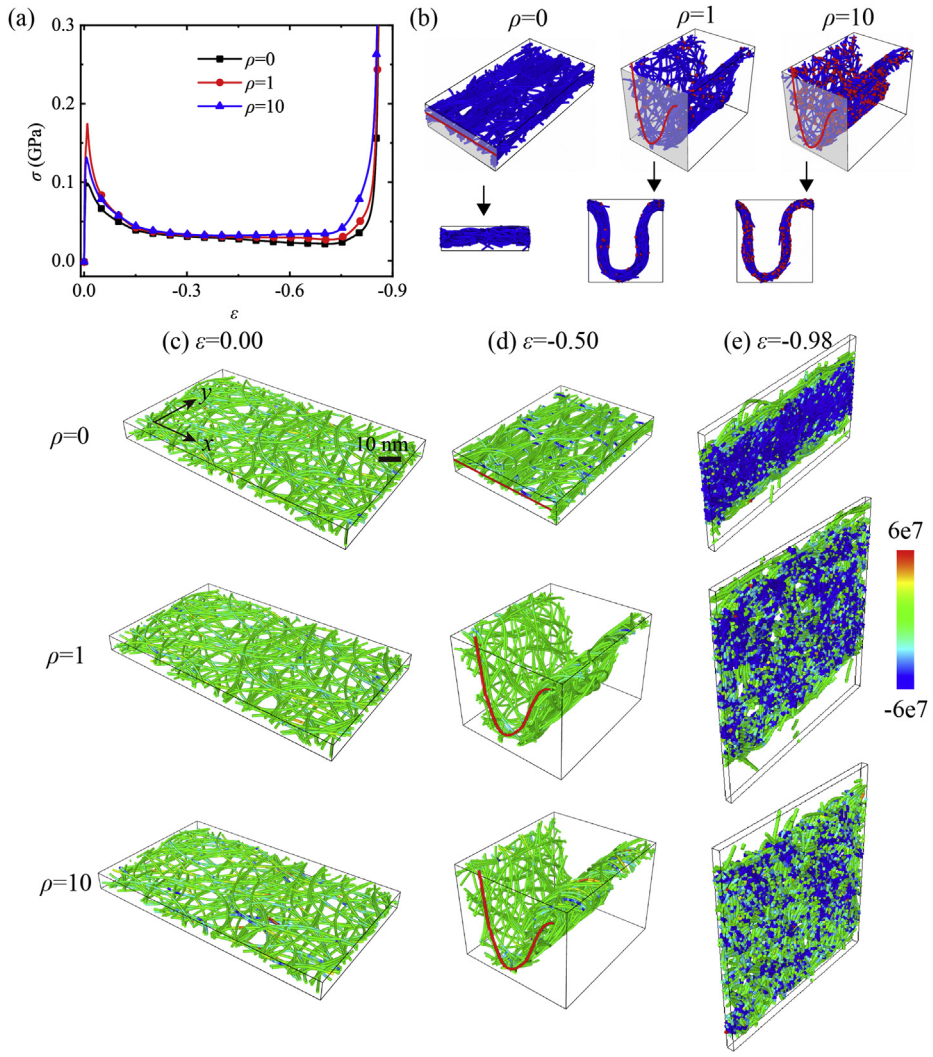

Fig. 3. The uniaxial compressive behavior of three buckypapers with $\rho = 0, 1$ and 10, respectively. (a) The stress-strain curves. (b) Typical morphologies for each structure. (c–e) the stress contours of σ_{xx} as the strain is increased from 0 to −0.98. (A colour version of this figure can be viewed online.)

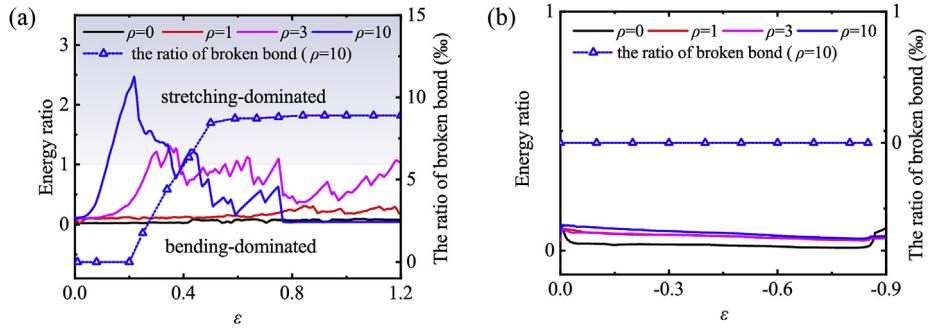

Fig. 4. The dominated deformation mode of the buckypapers. (a) The variations of the energy ratio and the ratio of broken bond under uniaxial tensile loading. (b) The variations of the energy ratio and the ratio of broken bond under uniaxial compressive loading. (A colour version of this figure can be viewed online.)

geometric reorganization. It is evident that the structure with $\rho = 1$ undergoes elastic-plastic deformation and ductile failure. For the buckypaper with a crosslink density of $\rho = 5$, the stress-strain curve moves forward and up compared with the curve of $\rho = 1$. There are still elastic stage, yield stage before the stress increases to a peak value, then a gradual damage stage after the peak value. The tensile stress decreases to 0 at the strain of about 0.65. Interestingly, there are several local stress peaks at the damage stage, which is similar to the stress of $\rho = 10$ structure in Fig. 2a. These local peaks have also been observed in porous materials like graphene foam [51], caused by stress redistribution after bonds break. According to the ratio of broken bond, the bond breaking occurs continuously from the yield stage at a strain of 0.25 to a full fracture at a strain of 0.65. Overall, the SCBP with $\rho = 5$ also undergoes elastic-plastic

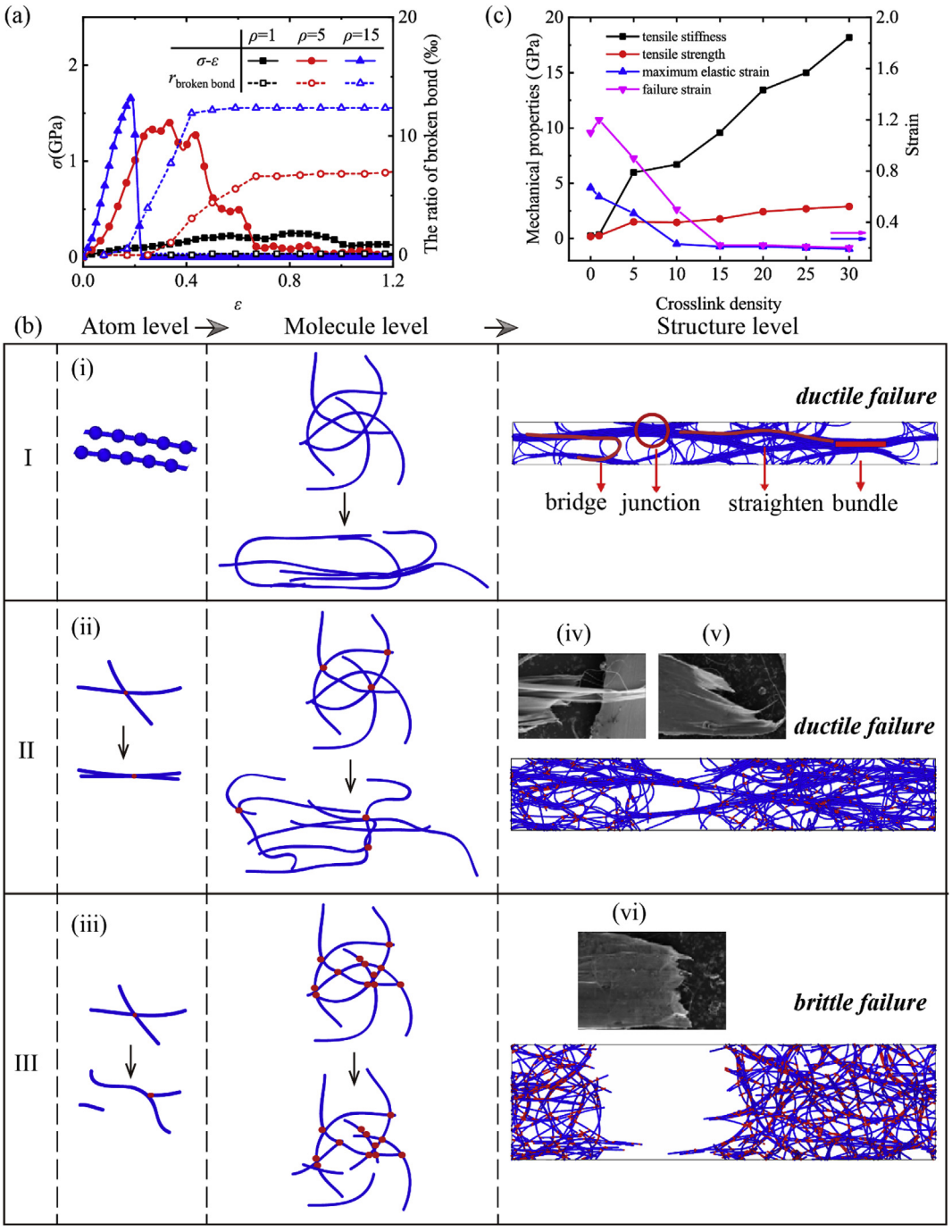

Fig. 5. The ductile-brittle transition mechanism under uniaxial tensile loading. (a) The stress-strain curves depict the ductile-brittle transition with three kinds of crosslink density of 1,5,15. The ratio of broken bond is used to interpret the failure process. (b) Microstructure evolution and analysis of the ductile-brittle transition mechanism. (b–i), (b-ii) and (b-iii) are atom level diagrams. (b-iv) and (b–v) [36] are ductile fracture of the buckypapers and (b-vi) [36] is brittle fracture image observed in experiments. (c) The effect of crosslink density on the mechanical properties, including tensile stiffness, tensile strength, maximum elastic strain, and failure strain. (A colour version of this figure can be viewed online.)

deformation and ductile failure, but it has stronger bearing capacity than the one with $\rho = 1$ and bond breaking occurs in the network. However, the system with a large number of crosslinks $\rho = 15$ has totally different stress-strain rule from the two above. The stress increases linearly and sharply at first, and then drops rapidly to 0 after reaching the peak value, which indicates a typical elastic-brittle fracture of the buckypaper. According to the curves of the ratio of broken bond, the SCBP of $\rho = 15$ breaks initially earlier than that of $\rho = 5$ at the same loading rate since it is prone to accumulate stress in the networks with a higher crosslinking degree. After the stress peak value at a strain of 0.18, the ratio rises sharply, leading to the brittle failure of the buckypaper. Finally, there are still some hysteretic bonds-breaking after the rapid loss of bearing capacity until the ratio stabilized to 12.5‰.

The ductile-brittle transition mechanism is analyzed by micro-structural hierarchical evolution in the atom-, molecular- and structure-level, shown in Fig. 5b. Three cases with different critical crosslink densities of 1, 5, 15 are discussed here, with corresponding

fracture modes of breaking-free ductile, ductile and brittle fracture. Type I includes buckypapers without ($\rho = 0$) or with low-density crosslinks ($\rho = 1$). In atom level, as shown in the sub-Fig. 5b–i, two adjacent carbon nanotubes are displayed in bead-chain model. There is no strong interaction between inter-molecule particles but only weak van der Waals force. In molecule level, since there is no strong restriction caused by crosslinks, entangled carbon nanotubes move freely and no drastic stress concentration appears with few bonds breaking. Most disordered molecule fragments align with the loading direction after being subjected to the external force. In structure level, several kinds of typical configurations maintain weak connections of the network, including straightened molecules, bridged molecules, bundles formed by many horizontal fragments of molecules, and strong junctions comprised of different bundles. As the increase of tensile strain, this weak connectivity weakens and induces the ductile failure of the buckypaper. As more crosslinks are added, the fracture mode of SCBP follows type II. In atom level, carbon nanotube molecules and crosslink are shown in blue and red in the sub-Fig. 5b–ii, respectively. The two CNTs strongly connected by crosslink cannot separate and gradually rotate around the crosslink to parallel to the loading direction. In molecule level, the local crosslink retention effect limits the free deformation of molecules and causes bond-breaking, leading to slow ductile fracture at the structure level. The ductile fracture of type I and type II occurs slowly and progressively, in which the fluffy fracture morphology with long-distance slippage and wavy pullout end of nanotubes indicate the easy sliding between contacting CNTs due to the weak intertube interaction in the highly porous structure. These characteristics are qualitatively consistent with the experimental observations shown in Fig. 5b–iv and b-v [36]. In Ref. [36], pristine buckypapers are prepared by the floating catalyst chemical vapor deposition (FCCVD) method, and crosslinks are generated by post treatments like the mechanical condensation or the mechanical condensation followed by acid treatment. The crosslink density is effectively controlled by the degree of post treatment. When there are massive crosslinks in the structure, as shown in type III, the intra or intertube chemical bonds bear intense stress because of the strong interaction and restriction caused by crosslinks, so they are prone to break rather than the rearrangement as shown in atom level diagram Fig. 5b–iii. In molecule level, due to the strong crosslink retention effect, it is difficult for molecules to deform and the topology of the network remains nearly unchanged in the whole loading process. In structure level, a large-scale stress concentration emerges and extends in the network, then extensive and violent fracture occurs suddenly in the structure after the SCBP meets the load-carrying limit with increasing strain. This brittle failure is featured by a neat brittle fracture cross-section, similar to the experimental results shown in Fig. 5b–vi [36], in which the tensile tests revealed that as more intertube interactions formed, the fracture morphologies changes from typical ductile featured by fluffy and wavy pullout end of nanotubes to a fairly straight brittle fracture surface.

The effect of the varied crosslink density of 0, 1, 5, 10, 15, 20, 25, 30 on some key mechanical parameters are investigated quantitatively as shown in Fig. 5c. With the increase of crosslink density, the stiffness raises almost linearly and the value added by 18 GPa after the crosslink density changes from 0 to 30. The tensile strength increases continuously and the value of $\rho = 15$ buckypaper is 16 times greater than that of the buckypaper without crosslinks. The maximum elastic strain drops remarkably at first, and then decrease slowly after the density is greater than 10. When $\rho \geq 15$, it keeps at a low value of 0.2 and changes little. During the whole tensile loading, the buckypaper without crosslinks is interconnected by weak van der Waals force, and finally breaks when the strain gets 1.1. After adding a merely small amount of crosslinks into buckypaper like $\rho = 1$, the structure can remain continuous. As more crosslinks are added, a great range of stress concentration appears and the bond-breaking occurs frequently which contributes to the fracture of the network, so the fracture strain declines monotonously. When the density is 15, the fracture strain almost has the same value with the maximum elastic strain, after that, the fracture strain barely changes, and keeps equal to the maximum elastic strain, which is also a sign that the material undergoes elastic-brittle failure at a certain crosslink density. Based on the above analysis, there is an obvious improvement in the bearing capacity as the crosslink density increases, but the network becomes more brittle. Therefore, in practical applications, it is necessary to choose an optimal crosslink density to obtain a compromise between the high strength and good ductility of the buckypapers.

3.4. The effect of the stiffness of CNT fiber and crosslinks

We also study the effect of the bending stiffness of CNT fibers on the mechanical properties of SCBP. Taking the value in Table 1 as the basic data (with a multiplier λ of 1), the parameter k_B which depends on the diameter of the constituent CNTs is zoomed from 0.1 to 10 to qualitatively examine the effect on the buckypaper with a given crosslink density. Fig. 6a displays the stress-strain curves of three structures with different bending stiffness under a tensile loading, where the crosslink density keeps as 10 indicating that all three structures follow the same elastic-plastic deformation mechanism. The key mechanical parameters are investigated quantitatively with varied zoom coefficient λ of 0.1, 0.5, 1, 5, 10 as shown in Fig. 6b. With the rising bending stiffness of the constituent CNTs, the tensile stiffness of buckypapers increases significantly, but maximum elastic strain and the fracture strain change slightly. Tensile strength of the buckypaper with $\lambda = 10$ is 4.7 times greater than that of the structure with $\lambda = 0.1$. Fig. 6c shows the initial and failure states of the buckypaper structures with $\lambda = 0.1, 1$ and 10, respectively. When the coefficient λ is 0.1, the structure is much easy to shrink to be a rope-like state during tension. As the zoom coefficient increases, *i.e.*, thicker CNT used, the structure gradually becomes solider and both structures with $\lambda = 1$ and 10 maintain a porous structure in tension. All these structures are tensioned to be broken as the tensile strain reaches ~0.5. In addition, the tensile stiffness k_T of the crosslinks has little effect on the mechanical properties of SCBP as shown in Fig. S10 in Supporting Information.

4. Conclusions

Coarse-grained molecular dynamics is used to study the mechanical mechanism of crosslinked buckypaper. We mainly focus on the effect of crosslinks on non-linear large-deformation behaviors of buckypaper. Firstly, the tensile strength of the buckypaper with $\rho = 10$ reaches 6 times higher than that of the buckypaper without crosslinks under the uniaxial tensile loading. Whereas in the process of compression, crosslinks have little effect on the enhancement of mechanical properties. As a result of crosslink retention effect, crosslinked buckypapers bends out of plane, different form in-plane deformation in non-crosslinked buckypaper. Moreover, the dominated deformation mode changes with increased crosslinks under the tensile loading. A critical crosslink density ρ_c divides the dominated deformation mode into two regimes, from a bending-dominated response at the crosslink density $\rho < \rho_c$ to a bending-stretching-bending three-stage response at $\rho > \rho_c$. This transition is attributed to the stress concentration and the intrinsic bond-breaking in large tensile

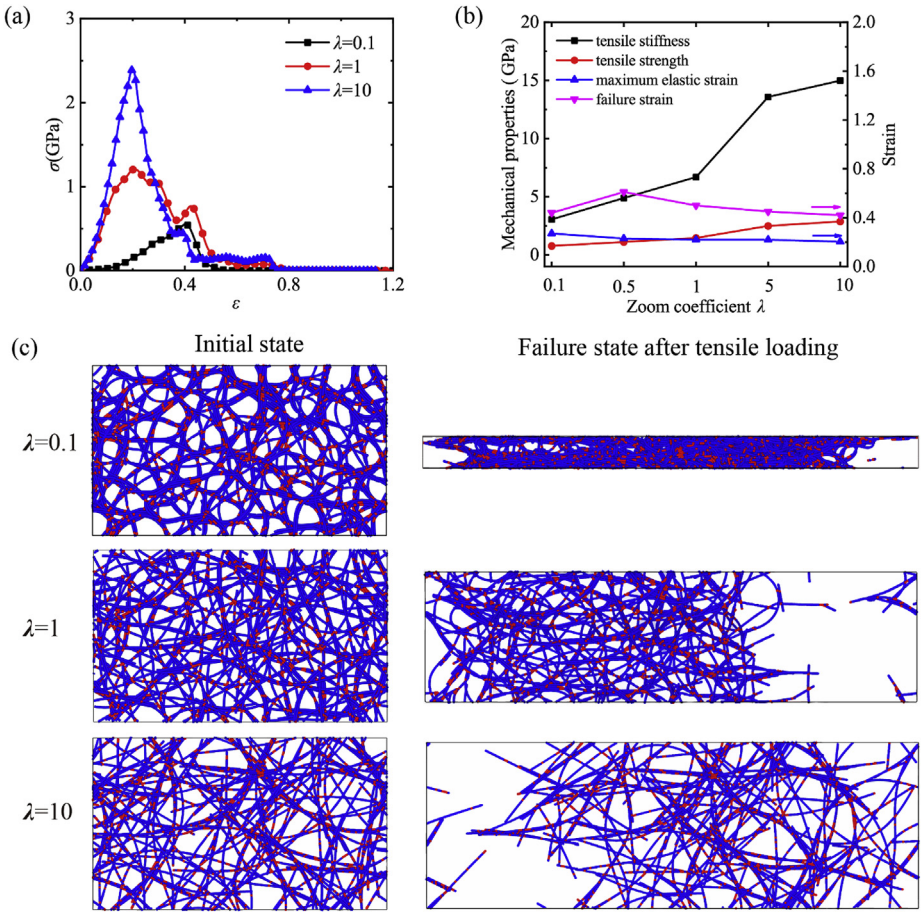

Fig. 6. The effect of bending stiffness on the mechanical properties. (a) The stress-strain relationship with the increase of bending stiffness. (b) The variation of mechanical properties with varied zoom coefficient of bending stiffness, including tensile stiffness, tensile strength, maximum elastic strain, and failure strain. (c) The initial and failure states of structures with different bending stiffness, including zoom coefficient λ = 0.1, 1 and 10. (A colour version of this figure can be viewed online.)

deformation. For a compressive loading, the buckypaper is bending-dominated throughout the whole loading process, independent on crosslinks. Remarkably, the ductile-brittle transition occurs as more crosslinks added, from ductile fracture in the structure with $\rho = 0$ and 1, to brittle fracture in buckypaper with a large number of crosslinks ($\rho = 10$). The mechanism behind this transition is analyzed through hierarchical microstructural evolution. Finally, the mechanical properties can be enhanced by improving the bending stiffness of constituent CNTs. This study indicates that crosslinks can be used to tune the mechanical performance, energy storage pattern and failure mode of buckypaper, which is of great significance for the understanding of basic mechanisms of buckypaper and optimization design of this promising material.

Author contributions

C.W. conceived the original idea, designed and supervised the simulations. T.Y. formulated the numerical model, conducted all simulations and drafted the paper. All authors reviewed the manuscript.

Notes

The authors declare no competing interest.

Acknowledgements

This work is supported by National Natural Science Foundation of China through Grants #11602270, #11972348 and Strategic Priority Research Program of the Chinese Academy of Sciences (Grants No. XDB22040503 and No. XDB22040403).

Appendix A. Supplementary data

Supplementary data to this article can be found online at https://doi.org/10.1016/j.carbon.2019.12.037.

References

[1] Y. Li, M. Kröger, A theoretical evaluation of the effects of carbon nanotube entanglement and bundling on the structural and mechanical properties of buckypaper, Carbon 50 (5) (2012) 1793–1806.
[2] R.L.D. Whitby, T. Fukuda, T. Maekawa, S.L. James, S.V. Mikhalovsky, Geometric control and tuneable pore size distribution of buckypaper and buckydiscs, Carbon 46 (6) (2008) 949–956.
[3] B. Kumanek, D. Janas, Thermal conductivity of carbon nanotube networks: a review, J. Mater. Sci. 54 (10) (2019) 7397–7427.
[4] J.G. Park, S. Li, R. Liang, X. Fan, C. Zhang, B. Wang, The high current-carrying capacity of various carbon nanotube-based buckypapers, Nanotechnology 19 (18) (2008) 185710.
[5] W.A.D. Wan Dalina, M. Mariatti, S.H. Tan, Z.A. Mohd Ishak, A.R. Mohamed, Fabrication and properties of multi-walled carbon nanotubes buckypaper, Adv. Mater. Res. 1108 (2015) 33–38.
[6] Y. Li, M. Kröger, Viscoelasticity of carbon nanotube buckypaper: zipping–unzipping mechanism and entanglement effects, Soft Matter 8 (30) (2012) 7822–7830.

[7] J. Zhang, D. Jiang, H. Peng, F. Qin, Enhanced mechanical and electrical properties of carbon nanotube buckypaper by in situ cross-linking, Carbon 63 (2013) 125–132.
[8] X. Liu, W. Lu, O.M. Ayala, L.P. Wang, A.M. Karlsson, Q. Yang, et al., Microstructural evolution of carbon nanotube fibers: deformation and strength mechanism, Nanoscale 5 (5) (2013) 2002–2008.
[9] S. Sharma, V. Kumar, A.K. Pathak, T. Yokozeki, S.K. Yadav, V.N. Singh, et al., Design of MWCNT bucky paper reinforced PANI–DBSA–DVB composites with superior electrical and mechanical properties, J. Mater. Chem. C 6 (45) (2018) 12396–12406.
[10] U. Tocoglu, O. Cevher, M.O. Guler, H. Akbulut, Coaxial silicon/multi-walled carbon nanotube nanocomposite anodes for long cycle life lithium-ion batteries, Appl. Surf. Sci. 305 (2014) 402–411.
[11] S. Roy, V. Jain, R. Bajpai, P. Ghosh, A.S. Pente, B.P. Singh, et al., Formation of carbon nanotube bucky paper and feasibility study for filtration at the nano and molecular scale, J. Phys. Chem. C 116 (35) (2012) 19025–19031.
[12] J. Chatterjee, J. Cardenal, A. Shellikeri, Engineered carbon nanotube buckypaper: a platform for electrochemical biosensors, J. Biomed. Nanotechnol. 11 (1) (2015) 150–156.
[13] Y. Yu, J.F. Zhai, Y. Xia, S.J. Dong, Single wearable sensing energy device based on photoelectric biofuel cells for simultaneous analysis of perspiration and illuminance, Nanoscale 9 (33) (2017) 11846–11850.
[14] J. Liu, A.G. Rinzler, H.J. Dai, J.H. Hafner, R.K. Bradley, P.J. Boul, et al., Fullerene pipes, Science 280 (5367) (1998) 1253–1256.
[15] C. Wang, Y. Li, L. Tong, Q. Song, K. Li, J. Li, et al., The role of grafting force and surface wettability in interfacial enhancement of carbon nanotube/carbon fiber hierarchical composites, Carbon 69 (2014) 239–246.
[16] P. Lv, Y. Feng, P. Zhang, H. Chen, N. Zhao, W. Feng, Increasing the interfacial strength in carbon fiber/epoxy composites by controlling the orientation and length of carbon nanotubes grown on the fibers, Carbon 49 (14) (2011) 4665–4673.
[17] J.N. Coleman, W.J. Blau, A.B. Dalton, E. Muñoz, S. Collins, B.G. Kim, et al., Improving the mechanical properties of single-walled carbon nanotube sheets by intercalation of polymeric adhesives, Appl. Phys. Lett. 82 (11) (2003) 1682–1684.
[18] Y. Cui, M. Zhang, Cross-links in carbon nanotube assembly introduced by using polyacrylonitrile as precursor, ACS Appl. Mater. Interfaces 5 (16) (2013) 8173–8178.
[19] K.H. Kim, Y. Oh, M.F. Islam, Graphene coating makes carbon nanotube aerogels superelastic and resistant to fatigue, Nat. Nanotechnol. 7 (9) (2012) 562–566.
[20] C. Wang, L. Wang, Z. Xu, Enhanced mechanical properties of carbon nanotube networks by mobile and discrete binders, Carbon 64 (2013) 237–244.
[21] M. Holzinger, J. Steinmetz, D. Samaille, M. Glerup, M. Paillet, P. Bernier, et al., [2+1] cycloaddition for cross-linking SWCNTs, Carbon 42 (5–6) (2004) 941–947.
[22] S. Wang, Z. Liang, B. Wang, C. Zhang, High-strength and multifunctional macroscopic fabric of single-walled carbon nanotubes, Adv. Mater. 19 (9) (2007) 1257–1261.
[23] M.B. Jakubinek, B. Ashrafi, J. Guan, M.B. Johnson, M.A. White, B. Simard, 3D chemically cross-linked single-walled carbon nanotube buckypapers, RSC Adv. 4 (101) (2014) 57564–57573.
[24] Z. Bo, H. Yang, P. Lv, J. Qian, K. Yu, G. Lu, et al., Covalently interconnected carbon nanotubes for enhanced charge transport in pseudocapacitors, Phys. Status Solidi B 252 (10) (2015) 2236–2244.
[25] A. Satti, A. Perret, J.E. McCarthy, Y.K. Gun'ko, Covalent crosslinking of single-walled carbon nanotubes with poly(allylamine) to produce mechanically robust composites, J. Mater. Chem. 20 (37) (2010) 7941–7943.
[26] Q.H. Do, C. Zeng, C. Zhang, B. Wang, J. Zheng, Supercritical fluid deposition of vanadium oxide on multi-walled carbon nanotube buckypaper for supercapacitor electrode application, Nanotechnology 22 (36) (2011) 365402.
[27] B. Xie, Y. Liu, Y. Ding, Q. Zheng, Z. Xu, Mechanics of carbon nanotube networks: microstructural evolution and optimal design, Soft Matter 7 (21) (2011) 10039–10047.
[28] S.W. Cranford, M.J. Buehler, In silico assembly and nanomechanical characterization of carbon nanotube buckypaper, Nanotechnology 21 (26) (2010) 265706.
[29] H. Chen, L. Zhang, J. Chen, M. Becton, X. Wang, H. Nie, Energy dissipation capability and impact response of carbon nanotube buckypaper: a coarse-grained molecular dynamics study, Carbon 103 (2016) 242–254.
[30] C. Wang, S. Chen, Viscoelastic properties of randomly entangled carbon nanotube networks under cyclic tension loading, Comput. Mater. Sci. 119 (2016) 46–51.
[31] Y. Ma, X. Yao, Q. Zheng, Y. Yin, D. Jiang, G. Xu, et al., Carbon nanotube films change Poisson's ratios from negative to positive, Appl. Phys. Lett. 97 (6) (2010), 061909.
[32] L. Berhan, Y.B. Yi, A.M. Sastry, E. Munoz, M. Selvidge, R. Baughman, Mechanical properties of nanotube sheets: alterations in joint morphology and achievable moduli in manufacturable materials, J. Appl. Phys. 95 (8) (2004) 4335–4345.
[33] Y. Chen, F. Pan, Z. Guo, B. Liu, J. Zhang, Stiffness threshold of randomly distributed carbon nanotube networks, J. Mech. Phys. Solids 84 (2015) 395–423.
[34] W. Ma, L. Song, R. Yang, T. Zhang, Y. Zhao, L. Sun, et al., Directly synthesized strong, highly conducting, transparent single-walled carbon nanotube films, Nano Lett. 7 (8) (2007) 2307–2311.
[35] F. Xu, B. Wei, W. Liu, H. Zhu, Y. Zhang, Y. Qiu, In-plane mechanical properties of carbon nanotube films fabricated by floating catalyst chemical vapor decomposition, J. Mater. Sci. 50 (24) (2015) 8166–8174.
[36] P. Liu, Y. Tan, D.C.M. Hu, D. Jewell, H.M. Duong, Multi-property enhancement of aligned carbon nanotube thin films from floating catalyst method, Mater. Des. 108 (2016) 754–760.
[37] S. Malik, H. Rösner, F. Hennrich, A. Böttcher, M.M. Kappes, T. Beck, et al., Failure mechanism of free standing single-walled carbon nanotube thin films under tensile load, Phys. Chem. Chem. Phys. 6 (13) (2004) 3540–3544.
[38] M. Yu, O. Lourie, M.J. Dyer, K. Moloni, T.F. Kelly, R.S. Ruoff, Strength and breaking mechanism of multiwalled carbon nanotubes under tensile load, Science 287 (2000) 637–640.
[39] Z. Wang, Chirality-dependent motion transmission between aligned carbon nanotubes, Carbon 151 (2019) 130–135.
[40] Z. Shen, M. Röding, M. Kröger, Y. Li, Carbon nanotube length governs the viscoelasticity and permeability of buckypaper, Polymers 9 (4) (2017) 115/1–115/18.
[41] C. Wang, E. Gao, L. Wang, Z. Xu, Mechanics of network materials with responsive crosslinks, Compt. Rendus Mec. 342 (5) (2014) 264–272.
[42] J. Ji, J. Zhao, W. Guo, Novel nonlinear coarse-grained potentials of carbon nanotubes, J. Mech. Phys. Solids 128 (2019) 79–104.
[43] S. Plimpton, Fast parallel algorithms for short–range molecular dynamics, J. Comput. Phys. 117 (1995) 1–19.
[44] A. Stukowski, Visualization and analysis of atomistic simulation data with OVITO-the open visualization Tool modelling, Model. Simul. Mater. Sci. Eng. 18 (2010), 015012.
[45] S. Cranford, H. Yao, C. Ortiz, M.J. Buehler, A single degree of freedom 'lollipop' model for carbon nanotube bundle formation, J. Mech. Phys. Solids 58 (3) (2010) 409–427.
[46] W.F. Van Gunsteren, H.J. Berendsen, Molecular dynamics: perspective for complex systems, Biochem. Soc. Trans. 10 (5) (1982) 301–305.
[47] S. Sakurai, F. Kamada, D.N. Futaba, M. Yumura, K. Hata, Influence of lengths of millimeter-scale single-walled carbon nanotube on electrical and mechanical properties of buckypaper, Nanoscale Res. Lett. 8 (1) (2013) 546–553.
[48] I.-W.P. Chen, R. Liang, H. Zhao, B. Wang, C. Zhang, Highly conductive carbon nanotube buckypapers with improved doping stability via conjugational cross-linking, Nanotechnology 22 (48) (2011) 485708.
[49] G.A. Buxton, N. Clarke, Bending to stretching" transition in disordered networks, Phys. Rev. Lett. 98 (23) (2007) 238103.
[50] D.A. Head, A.J. Levine, F.C. MacKintosh, Distinct regimes of elastic response and deformation modes of cross-linked cytoskeletal and semiflexible polymer networks, Phys. Rev. E 68 (6) (2003), 061907.
[51] D. Pan, C. Wang, T.C. Wang, Y. Yao, Graphene foam: uniaxial tension behavior and fracture mode based on a mesoscopic model, ACS Nano 11 (9) (2017) 8988–8997.